Influence of solvation on the spectral, molecular structure, and antileukemic activity of 1-benzyl-3-hydroxy-2-methylpyridin-4(1H)-one

Pheello Nkoe[a], Amanda-Lee E. Manicum[a*], Hitler Louis[b*], Frederick P. Malan[c], Wakopo J. Nzondomyo[a], Kelechi Chukwuemeka[b], Sibusiso A. Sithole[a], Ann Imojara[b], Chioma M. Chima[b], Ernest C. Agwamba[d,e] and Tomsmith O. Unimuke[b]

[a] *Department of Chemistry, Tshwane University of Technology, Pretoria, South Africa*

[b] *Computational and Bio-Simulation Research Group, University of Calabar, Calabar, Nigeria.*

[c] *Department of Chemistry, University of Pretoria, 02 Lynnwood Road, Hatfield, Pretoria 0001, South Africa*

[d] *Department of Chemistry, Covenant University, Ota, Nigeria*

[e] *Computational and Bio-Simulation Research Group, University of Calabar, Calabar, Nigeria*

[*]**Corresponding author's email**: louismuzong@gmail.com and ManicumAE@tut.ac.za

Graphical abstract

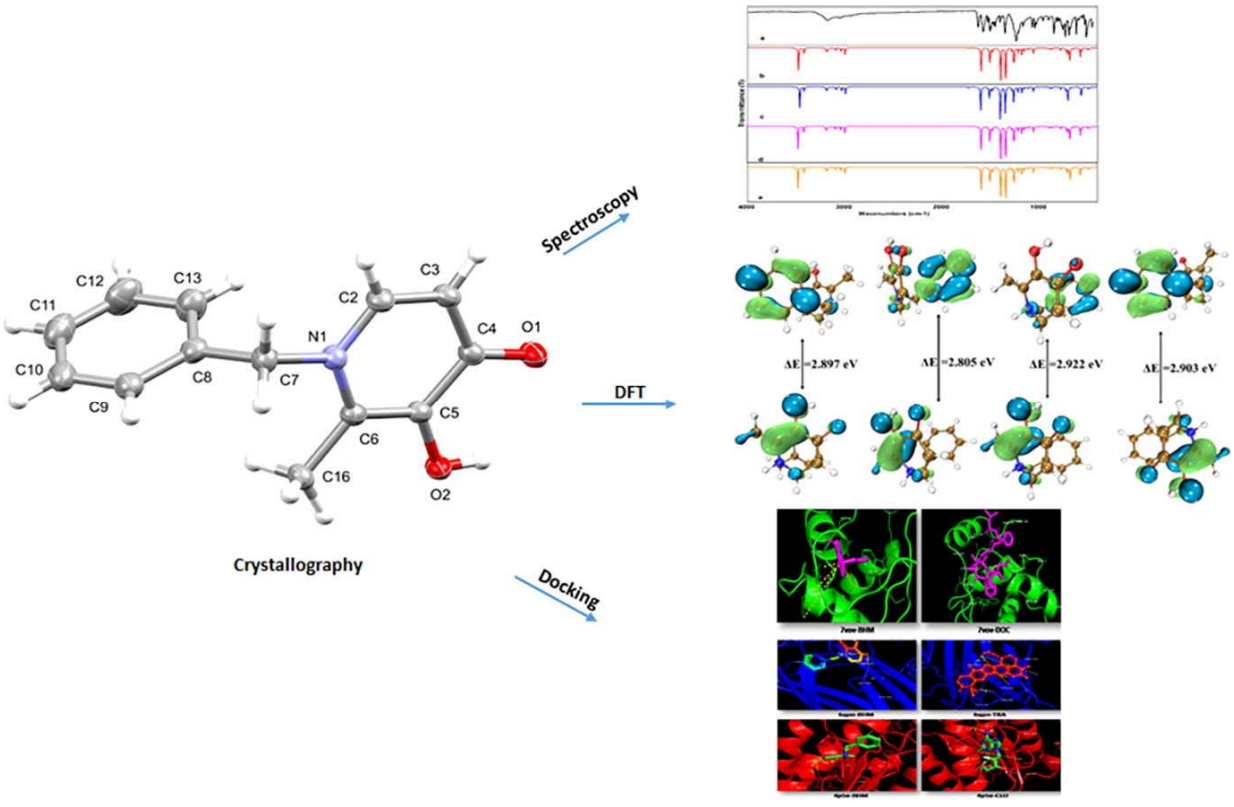

Abstract

This research focuses on the synthesis, X-ray crystallography, spectral characterization, and the influence of solvents on electronic molecular properties, vibrational analysis, and electronic excitation along with molecular modeling investigation of 1-benzyl-3-hydroxy-2-methylpyridin-4(1H)-one (BHM) as a potential anti-cancer agent. The electronic properties were investigated using density functional theory (DFT) computation at the B3LYP-GD3BJ/6-311++G(d,p) level in different electronic media: acetone, chloroform, ethanol, and water. The experimental wavenumbers of the 19 most pronounced infrared active bonds juxtaposed by the theoretical wavenumbers in four solvents namely acetone, chloroform, ethanol, and water with their corresponding theoretical intensities. Hirshfeld surface analysis reveals the major intermolecular interactions in the molecule are H···H, C···H, and O···H. The energy gap obtained from the four different solvents (acetone, chloroform, ethanol, and water) shows that BHM has higher reactivity in chloroform with an energy gap of 2.8055 eV as compared to acetone (2.8979 eV), ethanol (2.9035 eV) and water (2.9225 eV). In-silico molecular modeling showed that BHM possesses good anticancer potency with computed mean binding affinities of -3.8, -5.3, and -4.7 for the different tested leukemic targets and therefore, suggesting the applicability of BHM as an effective therapeutic agent for cancer.

Keywords: *1-benzyl-3-hydroxy-2-methylpyridin-4(1H)-one; X-ray crystallography; spectroscopy; solvents; DFT; molecular docking*

1.0 Introduction

Despite decades of severe basic medical practices in technical medicinal therapies, cancer has remained a major contributing cause of morbidity and mortality. This is a result of the wide complications encountered in identifying the viral cause of cancer as scientists have been engaged in dissecting the origins of human cancer and the relative role of genetic and epigenetic abnormalities. The most common choice of treatment for cancer includes surgery to remove cancer as much as possible, radiation therapy, and chemotherapy. Others also include bone marrow transplants, immunotherapy, hormone therapy, targeted drug therapy, and cryoablation. So many efforts and research studies have been carried out to curb the intensifying occurrence of cancer. Amina Tariq, et al., in 2019 (1) carried out research on the therapeutical potential of phosphorene

as a new drug delivery system to treat cancer. The study evaluated the potential of phosphorene as a drug delivery system for chlorambucil to treat cancer. The nature of the interaction between phosphorene and chlorambucil *via* a non-covalent interaction plot showed weak forces of interaction to be present between phosphorene and chlorambucil which is advantageous for easy unloading of the drug target. Results from the study confirmed phosphorene to possess significant therapeutic potential as a drug delivery system for chlorambucil to treat cancer. Rhoda et al., also in 2020 (2) did a study on gastric cancer cell line (MGC-803). The study incorporated molecular docking techniques and quantum chemical method *via* density functional theory (DFT) to predict the bioactivity of 1,2,3-triazole-pyrimidine derivatives against human gastric cancer cell line, MGC-803 as the receptor. Iqra et al., 2021 (3) for the first-time incorporated graphene as a carrier for daunorubicin for the treatment of cancer. The study implored the DFT method for the calculations of some physiochemical properties for the daunorubicin drug, graphene carrier, and daunorubicin-graphene complex. All calculations suggested graphene as an efficient carrier for the targeted delivery of daunorubicin for the treatment of cancer. To the best of the knowledge of the researchers, no study has been done on the anticarcinogenic potentials of 1-benzyl-3-hydroxy-2-methylpyridin-4(1H)-one (BHM) hence the need for this study.

In this study, the synthesis, spectroscopic characterization, and in-silico anti-cancer potency of BHM are investigated *via* experimental and computational approaches. The density functional theory method is applied to further highlight the reactivity and chemical nature of BHM. The synthesis of BHM was accomplished by Michael's addition of amine before aromatic ring activation and condensation to the desired product. Investigation of the electronic properties of BHM was made using the Frontier Molecular Orbital (FMO) analysis. The nature of inter- and intra-molecular charge transfer is also considered based on the Natural Bond Orbital Analysis. Furthermore, the Non-linear Optical Property was equally assessed. The spectroscopic characterization of BHM was accomplished by FT-IR, UV, NMR, and X-ray crystallography. Finally, a molecular docking study was done using BHM as a ligand against cancer proteins to further elucidate the anticarcinogenic potency of BHM.

2.0 Materials and Methods

2.1 Experimental

Reagents utilized to synthesize and characterize the products formed were purchased from Sigma Aldrich (South Africa) and were of analytical grade unless stated otherwise. The reagents and

organic solvents used for these experiments were not further purified or modified but were used as received. All the experiments were conducted in aerobic conditions using methanol. For infrared (IR) characterization, a PerkinElmer FT-IR Spectrometer Spectrum two, operating in the 4000 – 370 cm^{-1} region, was used to record the spectra. The IR is connected to a computer and has a built-in temperature cell regulator, accurate to 0.3 °C. All the IR spectra of the synthesized complexes were recorded at room temperature. A PerkinElmer Lambda XLS+ Ultraviolet/Visible (UV/Vis) spectrometer was used to collect the UV/Vis data using a 1.000±0.001 cm quartz cuvette cell. The Nuclear Magnetic Resonance (NMR) data were acquired from a Bruker MHz nuclear magnetic resonance spectrometer operating at 500.00 MHz for ^{1}H and ^{13}C at room temperature with deuterated dimethyl sulfide (DMSO-d6) as the solvent. Chemical shifts are reported in ppm relative to the DMSO-*d*6 (2.50 ppm on ^{1}H NMR and 39.52 ppm on ^{13}C NMR) peak. All coupling constants, *J*, are reported in Hertz (Hz).

2.1.1 Synthesis of 1-benzyl-3-hydroxy-2-methylpyridin-4(1H)-one (BHM)

Maltol (1.0060 g, 7.9771 mmol) and benzylamine (0.8548 g, 7.9771 mmol) were dissolved in 50 mL methanol. *p*-tolunesulfonic acid monohydrate (0.8548 g, 7.9771 mmol) was added and the reaction mixture was stirred at room temperature for 72 hours. *p*-tolunesulfonic acid monohydrate was filtered and the filtrate was left for evaporation, which resulted in yellow crystals. The schematic representation of the synthesized ligand is illustrated in **Scheme 1** below.

Yield = 1.6001 g, 93%; ^{1}H NMR (400 MHz, DMSO-d_6) δ (ppm): 7.78 - 7.73 (m, 1H), 7.41 - 7.26 (m, 3H), 7.10 - 7.04 (m, 2H), 6.23 – 6.18 (m, 1H), 5.25 (d, J = 5.0 Hz, 2H), 2.18 - 2.05 (m, 3H). ^{13}C NMR (400 MHz, DMSO-d_6) δ (ppm): 169, 145, 139, 138, 137, 129, 128, 127, 126, 111, 110, 56, 55, 40, 39, 38, 12, 11. IR (cm^{-1}): υ_{OH} = 3178, υ_{CH} = 3056, $\upsilon_{C=O}$ = 628, $\upsilon_{C=C}$ = 1577 and υ_{C-N} = 1233.

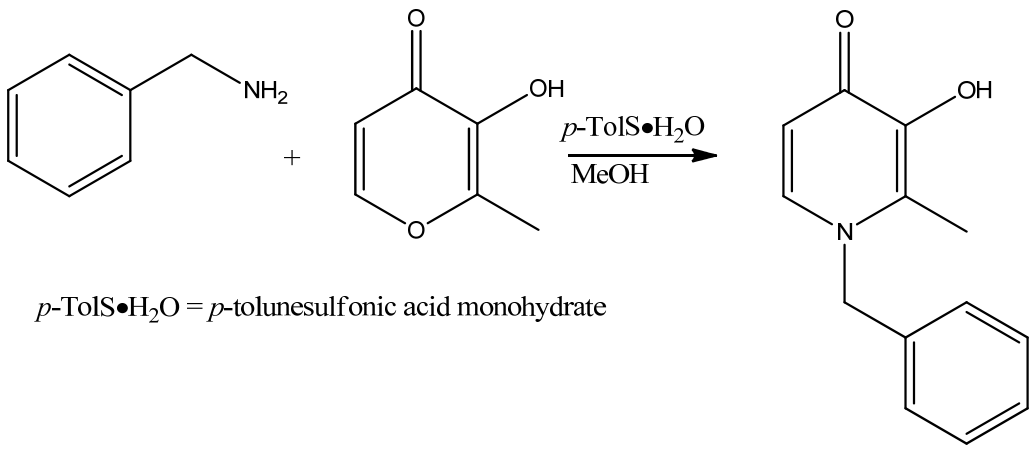

p-TolS•H_2O = *p*-tolunesulfonic acid monohydrate

Scheme 1: A schematic representation of ligand **BHM**.

2.1.2 Crystallography

Single crystals of 1-benzyl-3-hydroxy-2-methylpyridin-4(1H)-one (BHM) were analyzed on a Rigaku XtaLAB Synergy R diffractometer, with a rotating-anode X-ray source and a HyPix CCD detector. Data reduction and absorption were carried out using the CrysAlisPro (version 1.171.40.23a) software package (4). All X-ray diffraction measurements were performed at 150(2) K, using an Oxford Cryogenics Cryostat. All structures were solved by direct methods with SHELXTS-2013 (5) and refined using the SHELXL-2013 algorithm. All H atoms were placed in geometrically idealized positions and constrained to ride on their parent atoms. For data collection and refinement parameters, see Table S1 in the Supplementary information). The X-ray crystallographic coordinates for all structures have been deposited at the Cambridge Crystallographic Data Centre (CCDC), with deposition number CCDC 2214231. The data can be obtained free of charge from The Cambridge Crystallographic Data Centre *via* www.ccdc.cam.ac.uk/data_request/cif.

2.2 Computational details

2.2.1 Density Functional Theory (DFT)

To get the minimum energy configuration, ground state structural optimization of the synthesized compound was carried out using density functional theory (DFT). The popularly used B3LYP functional was employed along with the D3BJ dispersion term, and assigning DFT/6-311++G (d, p) basis set level of theory (6). All optimizations were carried out using Gaussian 16

software (7) coupled with its Gauss View6.0.16 inter-phase (56). The Highest Occupied Molecular orbital (HOMO) and the Lowest Unoccupied Molecular Orbital (LUMO) were carried out at the same function in different solvents to examine the stability and reactivity of the compound. Properties such as Non-linear optics (NLO) and Quantum descriptors such as the chemical hardness, softness, electron potential, and electrophilicity index have been calculated using Gaussian09W software (57) to evaluate the electronic behavior of the studied compound. Natural bond orbital (NBO) analysis has also been analyzed and extracted to gain insight into charge transfer and intra- and inter-molecular interactions. All Frontier Molecular Orbital (FMO) (HOMO and LUMO) iso-surface maps were plotted using the ChemCraft software (58) while the Hirschfield Surface analysis was done using Crystal Explorer version 3.1 (8). The VEDA was performed using Multwfn (9) and GaussView 6.0.16 while the spectra were plotted using Origin (59).

2.2.2 Molecular Docking Protocol

The molecular docking protocol as employed in this study involved the use of three major proteins involved in three different types of cancer namely: esophageal cancer, leukemia, and lung cancer with codes 6qpn, 4p5e, and 7vov respectively as obtained from the Protein Data Bank (PDB) (www.rcsb.org) from which their 3D geometric structures were downloaded (10-12). Whereas AutoDock Vina was used to performing the in silico molecular docking, the receptor-ligand interaction was visualized using Pymol (60) and Biovia Discovery Studio (61) following the preparation of the proteins by deleting the water and the native ligand groups in addition to adding polar hydrogen to enhance the efficiency of the interactions and most importantly, the SBD sites were defined at the x, y, z coordinates all in Biovia Discovery Studio which was used alongside AutoDock Vina (13) for the in silico docking. The anticarcinogenic potency of ligand, whose structural sketch was obtained with the aid of Gaussview 6.0.16 (56), was finally screened by interacting it with each of the four proteins aforementioned and compared with pharmaceutically established drugs medically recommended for each cancer type namely: TRA, CLO, and DEC downloaded from www.pubchem.ncbi.org complementarily. The relevant pictorial and tabulated results are presented in **Figure 8 & 9** and in **Tables 6 & 7**.

3.0 Results and discussion

3.1 Synthesis and molecular geometry

The ligand was synthesized *via* a single-step synthetic pathway in high yield, and this reaction involved Michael's addition of amine followed by the ring opening and ring closure as illustrated in Scheme 2. Mesomerisation of α,β-unsaturated carbonyl ligand cause β-carbon to be electron deficient and susceptible to nucleophilic attack. When primary amine is a nucleophile, there is a double attack at both α and β-unsaturated functions of the pyran-4-one leading to the formation of pyridine-4-one with the loss of a water molecule as illustrated in **Scheme 2**.

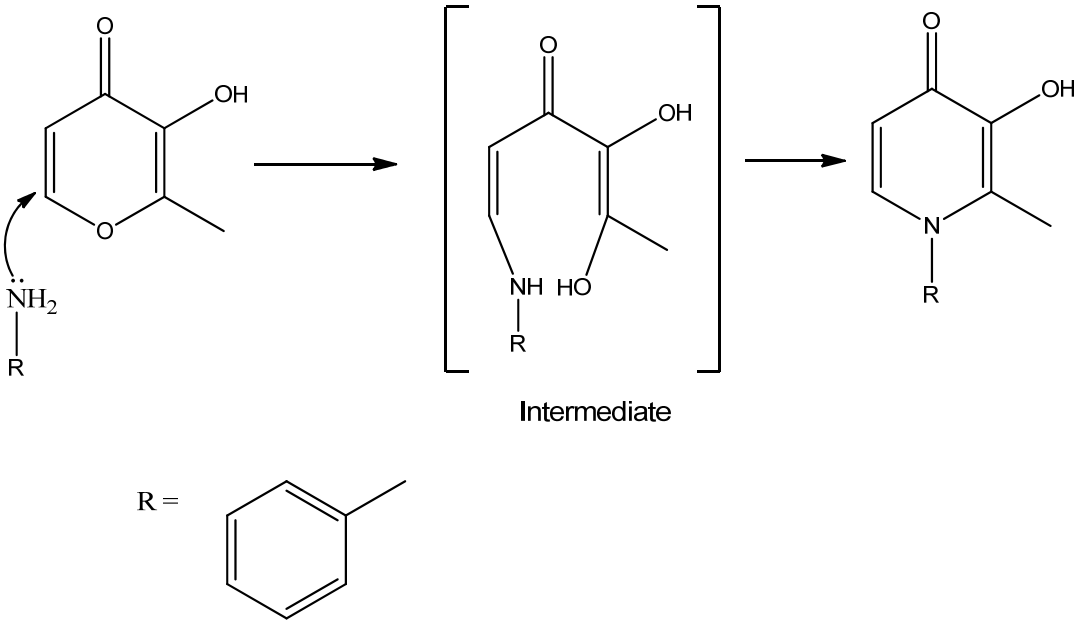

Scheme 2: Illustration of the formation of **BHM**.

The derivatives of pyranone conversions to the corresponding pyridinone analogs were achieved without protecting the hydroxyl group in methanol solvent *via* a one-step reaction, while this type of reaction in water is limited to the primary alkyl amines with a short chain length *i.e.* allylamine or ethylamine. The bulky alkyl amines with branched-chain give a low yield.

The structure was further confirmed and characterized with spectroscopic methods: IR, NMR, SCXRD, and UV/Vis. The maltol moiety shows two donor sites, i.e., the hydroxyl and the carbonyl oxygens. Distinct bands –OH, C–H (stretching), C=O, C=C, and C–N, appeared at 3178 cm^{-1}, 3056 cm^{-1}, 1628 cm^{-1}, 1577 cm^{-1}, and 1233 cm^{-1}, respectively (14, 15). The ^{1}H NMR was conducted on BHM in DMSO-*d*6, with a downfield shift of the methyl group on the maltol moiety

at 2.18 – 2.05ppm. The -CH_2 group is deshielded and appears at 5.25 ppm. The protons on the aromatic moiety appear in the known region 7.04 – 7.41ppm.

3.1.2 Crystal structure of 1-benzyl-3-hydroxy-2-methylpyridin-4(1H)-one (BHM)

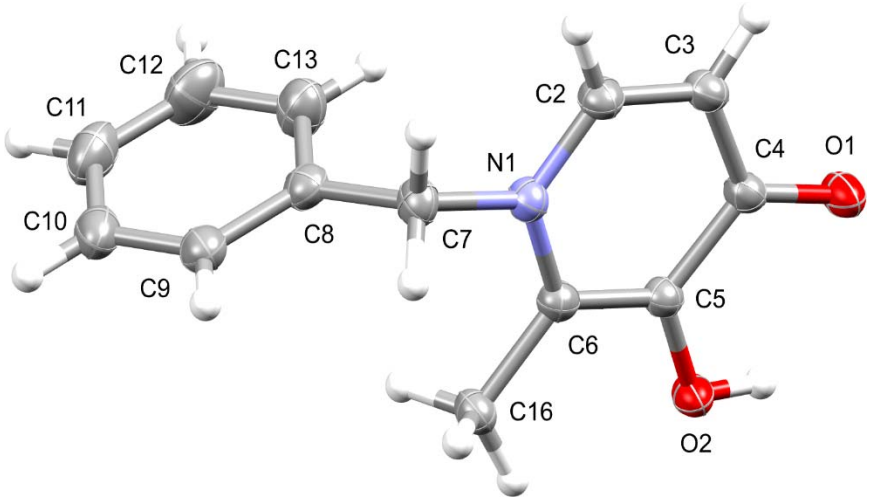

Figure 1: Molecular structure of BHM. Hydrogen atoms are omitted for clarity. Displacement ellipsoids are drawn at 50 % probability.

The ligand, 1-benzyl-3-hydroxy-2-methylpyridin-4(1H)-one (**BHM**), was obtained from a methanol solution. It crystallized in the monoclinic space group, $P2_1/c$, with four molecules in the unit cell (Z = 4). The molecular diagram of BHM is given in **Figure 1.** In general, the molecular structure confirms the coupling of the amine and oxime precursors to form BHM. The N-C7 bond length of 1.4705(18) Å corresponds to a C-N single bond. The diketonato-type moiety within the pyridinone ring is characterized by two unique bond lengths C4-O1 (1.2645(18) Å) and C5-O2 (1.3575(18) Å) (Table S1 in the SI). The plane of the arene ring intersects the pyridinone ring at an angle of *c.a.* 88.84°. All other bond lengths and angles are within the expected ranges.

There is also intra- and intermolecular hydrogen bonding present within BHM: a bifurcate O-H···O bond is present between O2-H2O and O1 (intramolecular) and between O2-H2O and O1 of an adjacent molecule (intermolecular) to result in the formation of a dimer (Figure S1 and Table S2 in the SI). Because of the simultaneous hydrogen bonding, non-ideal hydrogen bond donor and acceptor bond distances and angles are observed. Within the same molecule, O2-H2O···O1 is considered to be relatively weak as the interaction is at an angle of 113.72°, with an H···O distance of 2.273 Å. The intermolecular bond is stronger with a corresponding O2-H2O···O1 angle of 151.76° and an H···O distance of 1.936 Å.

Molecules of BHM pack in three dimensions to form arene-rich layers which are separated by pyridinone-rich layers (Figure S2 in the SI). Despite the high concentration of arene moieties throughout these layers, there were no pi-pi stacking interactions present within the structure. The adjacent arene groups are tilted independently to one another, with nearest-neighbor parallel arene groups situated > 7.2 Å from one another.

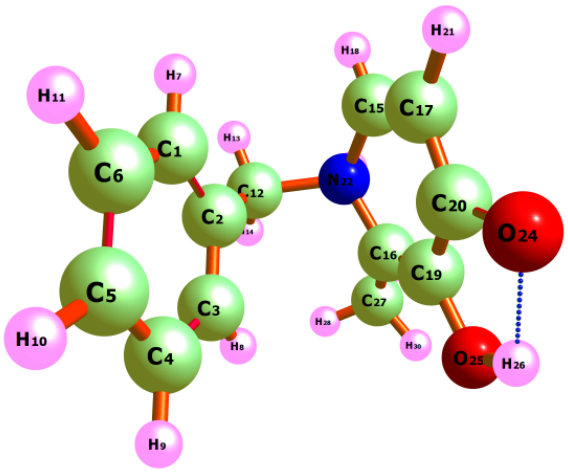

Figure 2: Optimized structure of 1-benzyl-3-hydroxy-2-methylpyridin-4(1H)-one (BHM). Relaxed structure is obtained at B3LYP-GD3BJ/6-311++G(d,p)

For computational modeling, the geometry of BHM has been modeled as depicted in **Figure 2** based on the crystallographic data and other spectroscopic characterization. To further understand the behavior of the synthesized ligand, computations of the molecular geometry were performed in different solvents. The values of the lattice constants of the studied compound are respectively shown in **Table 1**. The DFT (theoretical) lattice constants of the studied compound were calculated at the different solvents range between 1.391Å – 1.477Å; and 119.934^0 – 120.451^0. Likewise, for the experimental, the values of the lattice constants extracted at different solvents range from 1.359Å – 1.440 Å; and 115.211^0 to 122.431^0. This indicates that the values by DFT calculations well reproduce the experimental values as listed in **Table 1**.

Table 1: The geometrical parameters (bond length and bond angle) of BHM calculated at B3LYP-GD3BJ/ 6-311++ G (d p) level of theory.

	Theoretical				Experimental
Description	**Acetone**	**Chloroform**	**Ethanol**	**Water**	
			Bond Length (Å)		
$C_2 – C_3$	1.400	1.400	1.400	1.400	1.359
$C_3 – C_4$	1.392	1.391	1.392	1.392	1.423
$C_4 – C_5$	1.395	1.395	1.395	1.395	1.440
$C_5 – C_6$	1.395	1.395	1.395	1.395	1.367
$C_{16} – N_{22}$	1.476	1.476	1.476	1.477	1.384
			Bond Angle (^{0})		
$C_3– C_4 – C_5$	119.998	119.998	119.998	119.997	115.211
$C_4– C_5 – C_6$	119.938	119.956	119.938	119.934	122.431
$C_5– C_6 – C_1$	119.991	119.985	119.992	119.993	122.181
$C_2– C_1 – C_6$	120.451	120.447	120.451	120.451	120.351

3.2 Spectroscopic Characterization

3.2.1 NMR characterization

The ^{1}H NMR data obtained for BHM shows a downfield shift of the methyl group on the maltol moiety. The peak between 2.18 – 2.05 ppm is assigned to the methyl group on maltol moiety. The -CH_2 group is observed at 5.25 ppm and this peak is observed to be deshielded by the adjacent nitrogen and oxygen groups by inductive and anisotropic effects respectively. The spectra data for both ^{1}HNMR and ^{13}CNMR are reported in Figures S4 and S5 in the SI.

3.2.2 UV/Vis-characterization

The synthesized ligand was further characterized by UV/Vis spectroscopy. The obtained spectra are presented in Figures S6-S9 in the SI. The spectra obtained in different solvents show a characteristic peak around 310 nm to 350 nm. The absence of absorption in the visible region shows that BHM is colorless and undergoes $\pi \rightarrow \pi^*$ type excitation. Solvatochromism is observed to be minimal in the experimental spectrum.

3.2.3 Vibrational characterization

Fundamentally, FTIR has three comparative advantages in contrast to other spectroscopic analytical techniques owing to its speed, sensitivity, and internal calibration technically termed the Felgett, Jacquinot, and Connes advantages respectively (13). This is especially true of IR radiations within the mid-IR spectral range (4000 to 400 cm^{-1} or 1300nm) as it can induce molecular vibrations more efficiently resulting in the absorption bands specific to different functional groups as graphically depicted in the IR spectrograph. Hence, infrared radiation, which is largely thermal energy is mainly employed in the spectroscopic analysis of the molecular vibrations of chemical species, and the underlying principle is succinctly substantiated by Hooke's Law (16) i.e., the smaller mass is equivalent to the higher frequency of absorption and Badger's Rule i.e. the shorter the bond length of a group the higher the frequency of vibration (17).

Structurally, the ligand has 30 atoms hence, 144 normal modes as determined by the equation 3n-6 for a non-linear molecule, where n is the number of atoms. Of these normal vibration modes, only 88 were observed. The rest are non-observable bands hence, infrared inactive, a phenomenon which can be accounted for by either their weak polarity or their symmetrical nature (18). Of the 88 observable normal modes, 19 modes were prominently identified in the experimental IR spectra hence forming the basis of the functional group assignments and essentially the discussion. Moreover, as shown in the experimental spectra of these 19, 8 occurred within the functional group region and are the most pertinent in characterizing the molecule based whereas 11 were within the fingerprint region but were painstakingly identified and assigned as well. Summarily, both stretching (symmetric and asymmetric) and bending vibrations including scissoring (symmetric in-plane), rocking (asymmetric in-plane), twisting (symmetric out-of-plane), and wagging (symmetric out-of-plane) vibrations were observed. Additionally, as deducible from the nature of the IR spectra, the IR absorption bands can be classified as strong (s), medium (m), and weak (w) depending on the magnitude of transmittance but are mainly weak in this case.

Table 2 summarizes the experimental wavenumbers of the 19 most pronounced infrared active bonds juxtaposed by the theoretical wavenumbers in 4 solvents namely acetone, chloroform, ethanol, and water with their corresponding theoretical intensities. The unscaled wavenumbers are multiplied by a scale factor of 0.9668 to account for the theoretical shortcomings basically because the electronic structure calculation is approximate (19, 20) hence the necessity of increasing their closeness with the experimental wavenumbers. Furthermore, the choice of employing the scale

factor for this study done at the B3LYP-GD3BJ/6-311++G(d, p) computational method per previously reported scientific literature for scaling IR wavenumbers the Density Functional Theory method (21, 22). Although beyond the scope of this research, worthy of note is the apparent effect of solvent chemistry (mainly polarity) on IR spectral absorption (23, 24) as evident in the slight differences in the corresponding theoretical wavenumbers and intensities across the four solvents. The distinguishable absorption bands within the functional group region in the experimental IR peaked at 3178.40 cm^{-1}, 3054.50 cm^{-1}, 2940.00 cm^{-1}, 1627.50 cm^{-1}, 1576.70 cm^{-1}, 1506.70 cm^{-1}, 1452.70 $cm^{-1,}$ and 1401.90 cm^{-1}. The 3178.40 cm^{-1} wavenumber corresponds to the symmetric O-H stretching vibrations. This is in tandem with the typical O-H stretching vibrations wavenumber range for aromatic compounds (25) and was further confirmed in the theoretical wavenumbers (scaled) of 3361.89cm^{-1}, 3348.90cm^{-1}, 3478.09$cm^{-1,}$ and 3364.99cm^{-1} for the four solvents: acetone, chloroform, ethanol, and water respectively. As shown in **Table 2**, the intensity of this absorption in the theoretical spectra was greatest in water with an IR intensity of 277.57. Symmetrical N-H stretching was observed at the 3054.50 wavenumbers. In the theoretical study, this was observed at 3306.59 cm^{-1}, 3306.45 cm^{-1}, 3306.58 cm^{-1}, and 3306.52 cm^{-1} across the four solvents and is well in line with previously published data on symmetrical N-H vibrations of aromatic compounds (26). The 2940.00 cm^{-1} wavenumber corresponds to symmetrical sp^3 C-H stretching as corroborated in previous research works (27). The theoretical wavenumbers were slightly lower in all four solvents with wavenumbers being lowest in chloroform at a magnitude of 2893.55 cm^{-1} followed by acetone with a magnitude of 2898.86 cm^{-1}. The corresponding scaled frequencies in ethanol and water were 2899.15 cm^{-1} and 2900.11 cm^{-1} respectively with acetone and chloroform having the highest and lowest IR intensities of 82.18 and 80.90 respectively. The experimental 1627.50 cm^{-1} wavenumber occurs within the aromatic overtones range (27) but equally coincides with the asymmetric C-H bond deformation (bending vibration). In the theoretical spectra, this peaked at lower values with chloroform and water having the highest and lowest wavenumbers of 1589.13 cm^{-1} and 1588.62 cm^{-1} respectively. In ethanol, this was observed at 1588.69 cm^{-1} whereas in acetone it peaked at 1588.71 cm^{-1}. The symmetrical C=C stretching vibrations are assigned to the two experimental wavenumbers in the 1500 range in line with the literature (28). At the 1576.70 cm^{-1} wavenumber, the absorption was medium whereas in the 1506.70 cm^{-1} wavenumber it was weak. In the former, the theoretical wavenumbers were lower with correspondingly high IR intensities as shown in **Table 2**.

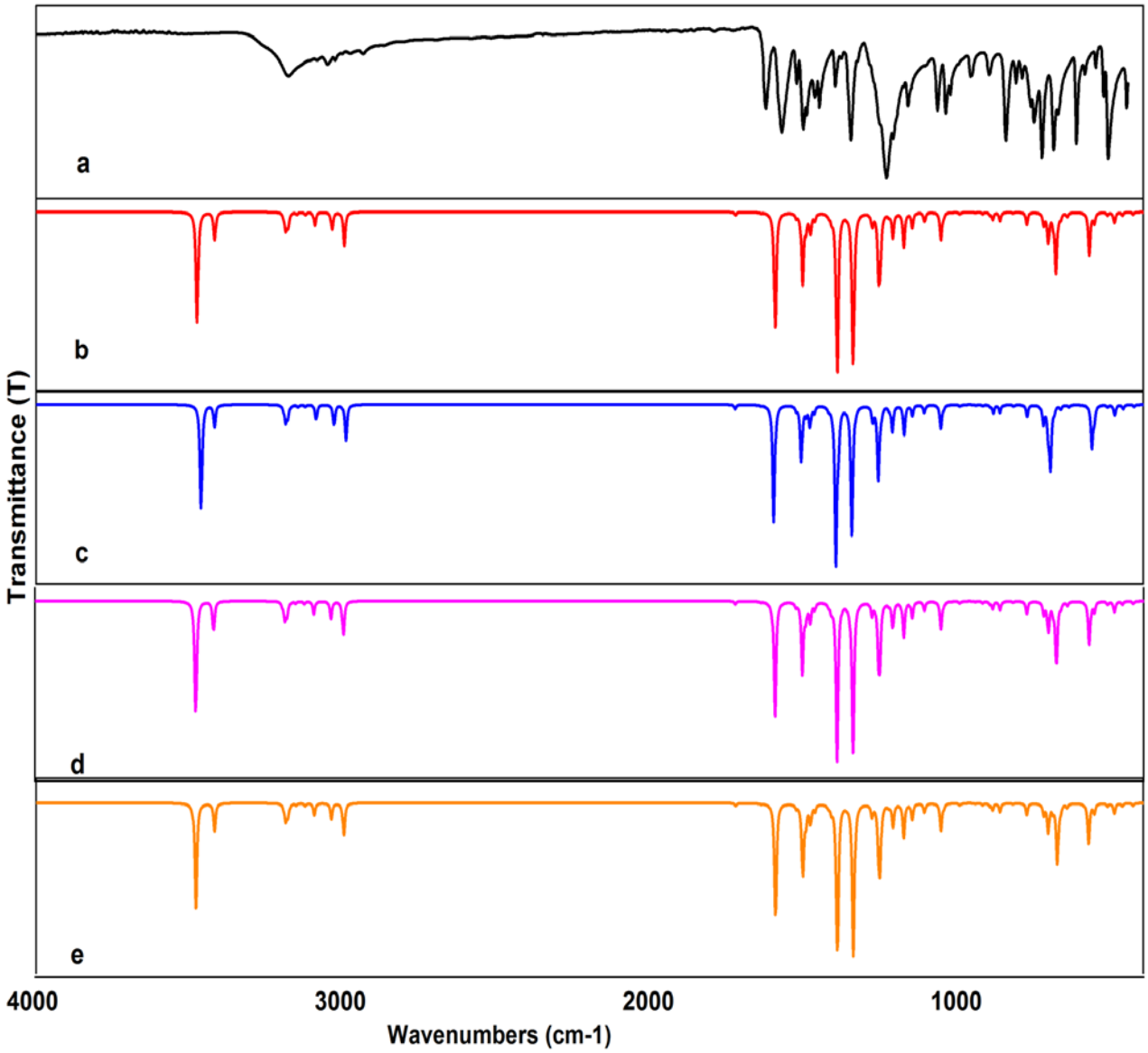

Figure 3: FT-IR spectra: 'a' is experimental whereas 'b-e' denote the theoretical in acetone, chloroform, ethanol, and water respectively.

Chloroform was highest at 1548.73 cm^{-1} whereas water had the lowest at a wavenumber of 1543.25 cm^{-1}. In the latter i.e. the 1506.70 cm^{-1} wavenumber, the C=C symmetrical stretching occurred at complementarily lower wavenumbers across the four solvents: acetone, chloroform, ethanol, and water with magnitudes of 1458.44 cm^{-1}, 1462.22 cm^{-1}, 1458.21 $cm^{-1,}$ and 1457.45 cm^{-1} respectively with correspondingly high IR intensities as captured in **Table 2**.

Table 2: Experimental and theoretical absorption frequencies and IR Intensities of BHM.

MODES	EXPERIMENTAL	THEORETICAL												ASSIGNMENT
		ACETONE			CHLOROFORM			ETHANOL			WATER			
	F (cm^{-1})	F^a (cm^{-1})	F^b (cm^{-1})	I	F^a (cm^{-1})	F^b (cm^{-1})	I	F^a (cm^{-1})	F^b (cm^{-1})	I	F^a (cm^{-1})	F^b (cm^{-1})	I	
S1	3178.40 w	3477.34	3361.89	269.13	3463.90	3348.90	235.25	3478.09	3362.62	271.10	3480.54	3364.99	277.57	ν_sOH
S2	3054.50 w	3420.14	3306.59	67.58	3419.99	3306.45	49.27	3420.13	3306.58	68.72	3420.07	3306.52	72.50	ν_sNH
S3	2940.00 w	2998.41	2898.86	82.18	2992.91	2893.55	80.90	2998.71	2899.15	82.12	2999.70	2900.11	82.14	ν_sCH
S4	1627.50 w	1643.27	1588.71	1.77	1643.70	1589.13	1.54	1643.25	1588.69	1.78	1643.17	1588.62	1.82	β_{asym}CH
S5	1576.70 m	1597.30	1544.27	285.83	1601.91	1548.73	265.15	1597.06	1544.04	286.66	1596.25	1543.25	289.17	ν_sCC
S6	1506.70 w	1508.52	1458.44	172.13	1512.43	1462.22	125.88	1508.28	1458.21	174.45	1507.50	1457.45	181.21	ν_sCC
S7	1452.70 m	1497.23	1447.52	34.94	1496.88	1447.18	17.42	1497.24	1447.53	36.73	1497.27	1447.56	43.70	γ CH
S8	1401.90 w	1468.41	1419.66	16.83	1470.36	1421.54	15.13	1468.29	1419.54	16.92	1467.91	1419.18	17.26	γ CH
S9	1351.00 m	1364.24	1318.94	2.23	1363.58	1318.31	2.14	1364.28	1318.99	2.24	1364.41	1319.11	2.27	ρ CH
S10	1233.40 m	1256.39	1214.68	112.17	1254.58	1212.93	22.51	1256.41	1214.70	121.33	1256.42	1214.71	152.00	τ CH
S11	1166.70 w	1179.25	1140.10	72.11	1180.35	1141.16	0.88	1179.30	1140.15	77.16	1179.50	1140.34	85.51	τ CH
S12	1071.30 w	1111.90	1074.98	22.07	1112.42	1075.49	17.56	1111.87	1074.96	22.34	1111.78	1074.87	23.27	ρ CH
S13	1042.70 w	1058.01	1022.88	45.67	1058.15	1023.02	32.37	1058.00	1022.87	46.77	1057.95	1022.83	50.62	β C=C
S14	960.10 w	990.33	957.45	0.82	988.39	955.58	0.61	990.44	957.56	0.84	990.76	957.87	0.90	τ CH
S15	902.89 w	923.02	892.38	4.34	922.69	892.06	2.92	923.03	892.39	4.43	923.06	892.41	4.76	ρ CH
S16	848.86 m	866.49	837.72	21.75	866.71	837.94	17.49	866.48	837.71	22.01	866.42	837.65	22.87	β CH
S17	693.13 m	724.33	700.28	29.44	725.28	701.20	40.78	724.33	700.28	29.22	724.33	700.28	28.62	δ CH
S18	620.03 m	647.34	625.85	9.15	642.09	620.77	4.88	647.57	626.07	9.28	648.28	626.76	9.52	δ CH
S19	515.15 m	559.95	541.36	23.92	559.86	541.27	24.82	559.93	541.34	24.04	559.88	541.29	24.48	β_{asym} C=C

$F(cm^{-1})$ is the experimental frequency; F^a (cm^{-1}) is the theoretical un-scaled frequency; F^b (cm^{-1}) is the theoretical scaled frequency; I is the intensity of absorption; τ denotes symmetrical twisting; β_{asym} denotes asymmetrical bending; β denotes symmetrical bending; γ denotes scissoring δ denotes aromatic out-of-plane deformation; ν_s denotes symmetrical stretching; w and m denote weak and strong absorption bands respectively.

However, it should be noted that the complementary unscaled theoretical frequencies at the 1506.70 cm^{-1} experimental wavenumber were way closer to the experimental value than the scaled frequencies. The sp^3 C-H scissoring vibration was observed at two absorption bands in the experiment: 1452.70 cm^{-1} and 1401.90 cm^{-1} respectively. This assignment is scientifically backed by previously published works and further accentuated by the complementary theoretical wavenumbers as equally presented clearly in **Table 2**. From the scaled frequencies, it can be observed that at the 1452.70 cm^{-1} experimental wavenumber the corresponding value in water was closest at 1447.56 cm^{-1} followed by ethanol and acetone where this peak was observed at 1447.53 cm^{-1} and 1447.52 cm^{-1} respectively while chloroform had the lowest at 1447.18 cm^{-1}. The scaled theoretical wavenumbers for the 1401.90 cm^{-1} C-H scissoring were slightly higher in magnitude by approximately a score. The value across the four solvents was not deviant from the previously established range (28) and was highest in chloroform where it peaked at 1421.54 cm^{-1} and lowest in water with a scaled wavenumber of 1419.18 cm^{-1}.

3.3 Hirschfield Surface analysis

The molecular Hirschfield surface for the studied ligand has been examined using Crystal Explorer 3.1 program. The Hirschfield surface generated was done using a standard surface resolution with 3-D d_{norm} surface that is mapped over a fixed color scale of -0.6179 (red) to 1.1480 Å (blue), and a shape index that is mapped in the color range of -1.000 to 1.000 Å as presented in **Figure 4**. As displayed in **Figure 4**, it is observed that the dark red color indicates the H···H, O···H and C···H interactions, the other visible spots as observed in the surface shows the C···C, H···C and H···O contacts (29-31). Also, as observed from the **Figure 4**, the white color represents the intermolecular distance that is close to the Van der Waals contact. In order to examine the main intermolecular contact, the 2-D finger plots was generated and represented as **Figure 5**. As observed in **Figure 6**, the major intermolecular interactions in the molecule are H···H, C···H, O···H. Contribution of H···H contact to the total surface is 54.0%, the Contribution of C···H contact to the total surface is 11.5%, the Contribution of O···H contact to the total surface is 10.5%, with other contacts making up the remaining percentage contribution of the whole surface.

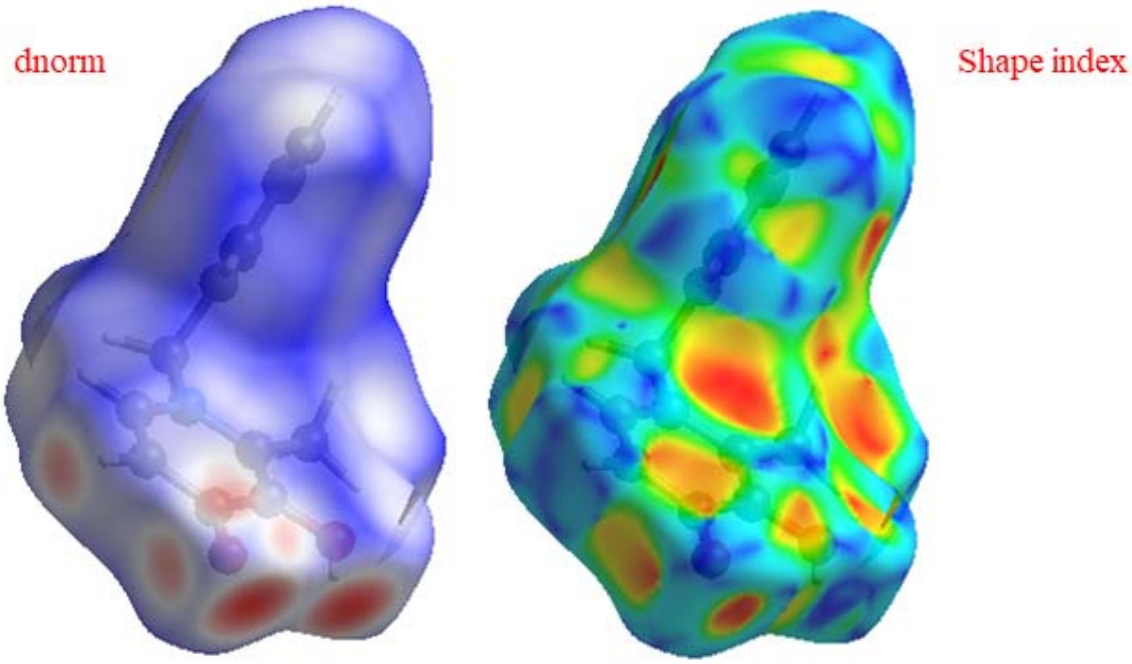

Figure 4: Visualization of 3-D d_{norm} surfaces for the studied ligand mapped over a fixed color scale of -0.6179 (red) to 1.1480Å (blue) and shape index.

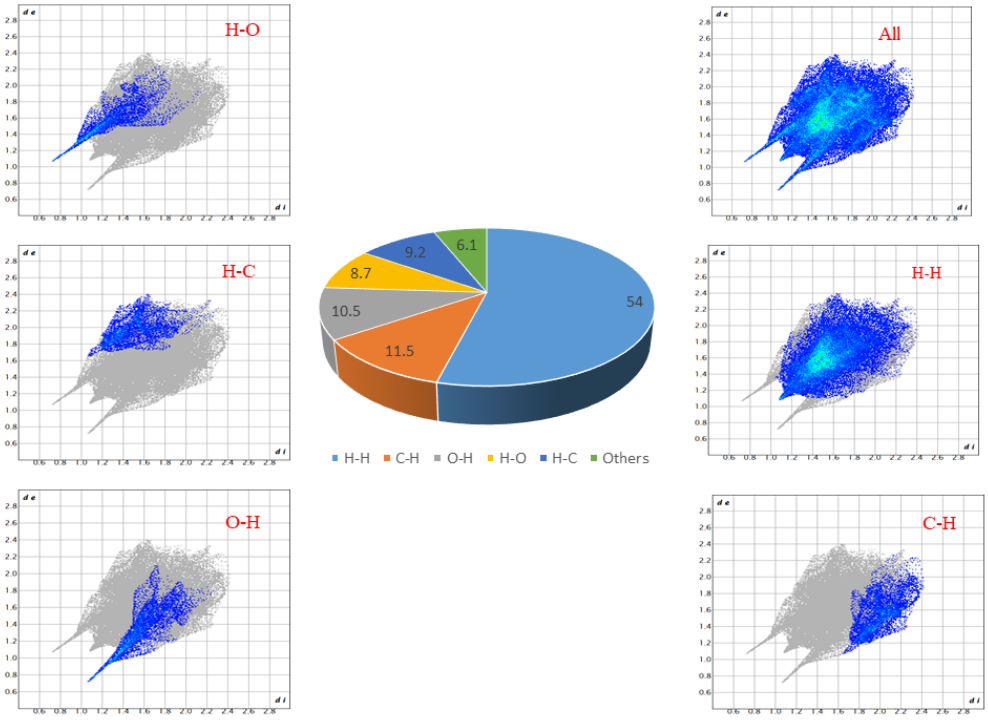

Figure 5: Visualization of 2-D Finger plots for BHM.

Intramolecular Interactions Analysis

In order to determine the atoms making up the studied ligand, the intramolecular interaction of the Hirshfeld surface have been obtained using Crystal Explorer 2.1 software (8). Since chemical bonds are considered to be intramolecular and are stronger than intermolecular interactions, that are present between atoms or molecules that are not bounded. Visualization of the studied ligand is depicted as **Figure 6**. It is observed that the strong intramolecular interactions within the ligand are between H-O bond.

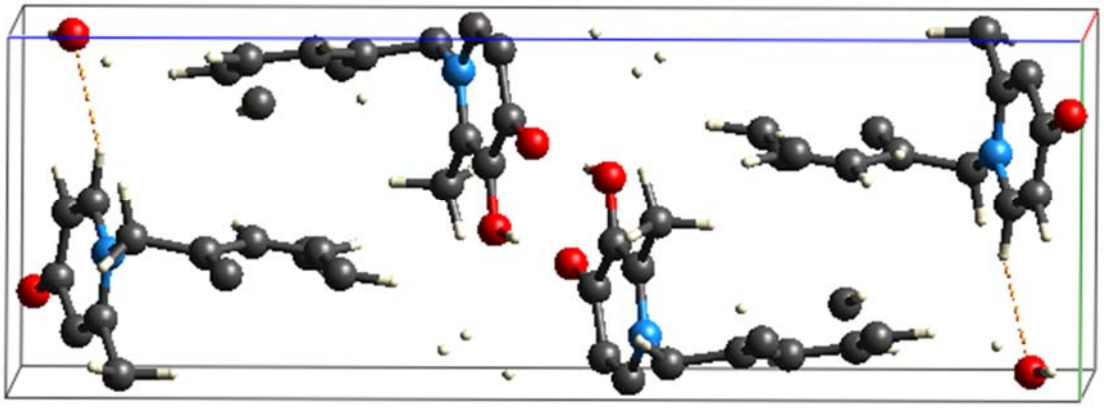

Figure 6: Intramolecular Interaction of BHM.

3.3 Electronic Properties

3.3.1 Frontier molecular orbital (FMO) analysis

The Frontier molecular orbital (FMO) analysis provides a platform for understanding the local reactivity of molecules. These molecular orbital plays very important role in the optical and electronic properties, pharmaceutical studies luminescence UV-VIS, quantum chemistry as well as providing information on the biological mechanism of a given compound. Furthermore, the FMO analysis helps to determine the most reactive position of a molecule. In order to study a chemical reaction only two molecular orbital HOMO (highest occupied molecular orbital) and LUMO (lowest unoccupied molecular data) are of great interest as laid down by Fukui. While the HOMO provides basic information on the electron donor characteristics (nucleophilic site) and the electron rich portion of the molecule, the LUMO shows the electron receptor characteristics of the molecule (electrophilic site) and the electron deficient portion of the molecule. Solvents are substances in which solute is dissolved and forms solution. Most times, the reactivity of a molecule is influenced by the solvent in which it is dissolved in (32)

herein, the energy gap, quantum descriptors such as global hardness and softness, chemical potential, electronegativity, electrophilicity index were obtained using the B3LYP/ 6-311 ++ G(d, p) basic set and Calculations were carried out based on the Koopmans theorem as reported in previous literature (33).

The energy gap (Δ**E**) which is obtained from the difference between the HOMO and LUMO supports to determine the stability and chemical reactivity of the compounds. The energy gap obtained from the four different solvents (acetone, chloroform, ethanol and water) shows that BHM has higher reactivity in chloroform with an energy gap of 2.8055 eV as compared to acetone (2.8979 eV), ethanol (2.9035 eV) and water (2.9225 eV). The result obtained shows that BHM is more reactive in chloroform and more stable in water. The reactivity order for BHM is chloroform> acetone> ethanol and water. Also, it is worthy to note that the solvent has little to no effect on the reactivity of BHM as the difference in the energy gap lies between 0.025 eV - 0.117 eV. This implies that the studied compound has high chemical reactivity (reveals the possibility of charge transfer within the molecule), biological activity and possibly polarizability. Furthermore, **Figure 7** shows the HOMO- LUMO plots in each solvent. The inference from these plots is that there is little or slight change in energy gap for BHM in each solvent. The LUMO is basically centralized on the benzene ring containing two oxygen atoms, while the HOMO is centralized on the second benzene ring with no oxygen. Also, from the plot, electrons are evenly distributed in each solvent.

Table 3: HOMO – LUMO, Energy gap and the relative global reactivity index calculated at the B3LYP-GD3BJ/6-311++ G (d p) level of theory.

Solvents	**HOMO eV**	**LUMO eV**	**ΔE**	**η**	***S***	**χ**	**μ**	**Ω**
Acetone	-3.937	-1.039	2.897	1.448	0.345	2.488	-2.488	1.244
Chloroform	-3.869	-1.063	2.805	1.402	0.356	2.466	-2.466	1.233
Ethanol	-3.942	-1.039	2.903	1.451	0.344	2.491	-2.491	1.245
Water	-3.956	-1.034	2.922	1.461	0.342	2.495	-2.495	1.247

Furthermore, to obtain the energetic properties of the compound in different solvents, the quantum chemical parameter such as chemical potential (μ), electro negativity (χ), electrophilicity index (ω) global hardness (η) and softness (S) were obtained. The chemical hardness of a molecule refers to the ability of a molecule to gain electron. The chemical softness, however, is the ability of a molecule to receive electron and is referred to as the

opposite of the chemical hardness. High chemical hardness value of 1.4613 eV is observed in water while a low value of 1.4027 eV is obtained in chloroform. The highest chemical softness value is obtained in chloroform (0.3564 eV), while the lowest is observed in water (0.3421 eV). The lower softness value obtained in all media indicates less polarizability of molecule. This result is in conformity with that obtained from the energy gap which suggests that BHM is stable in water and more reactive in chloroform. In addition, a high global softness value of 0.3564 eV and low value of 0.3421 eV strengthens the assertion made from the obtained energy gap results.

3.2.3 Natural bond orbital (NBO) analysis

When Lewis and non-Lewis type donor and acceptor interactions are present in molecular systems, natural bond orbital (NBO) analysis is extremely effective at estimating molecular stability (34). It allows one to investigate a compound's chemical properties, including intra- and intermolecular charge transfer, basicity, stability, reactivity, and the relationship between the donor and acceptor orbital, in terms of bonding, antibonding (donor-acceptor), and delocalization interactions (35). Additionally, NBO analysis uses the second order perturbation theory to explain a number of features, including the nature of Lewis donor and non-Lewis acceptor orbital and stabilization energy (36, 37). The information provided by the natural bond orbital investigation includes conjugative interaction, hyper-conjugative interaction, intramolecular hydrogen bonding, and intermolecular hydrogen bonding in a molecule (38). NBOs are a useful tool for comprehending the delocalization of electron density because they offer a valence bond-type description of the wave function that is closely related to concepts from classical Lewis structure.

The Lewis-like molecular bonding pattern of electron pairs (or of single electrons in the case of open-shell molecules) is best described by NBO analysis in a compact manner. The interaction between the donor and the acceptor in the NBO analysis is defined by a significant energy $E^{(2)}$ (39). Increased stabilization capacity $E^{(2)}$ reveals a greater tendency for intramolecular interactions between the donor and acceptor orbital, which may be attributed to a high capacity for giving electrons and a high degree of conjugation (40). Herein, The NBO computations were achieved with the same method and basis set employed for geometry optimization. The ten most prevalent interactions in various solvents (acetone, chloroform, ethanol and water), are provided in **Table 4** with regard to the second order perturbation energy. This table lists the energy $E^{(2)}$ between the local orbital which are the occupied bonding orbital BD, the empty anti bonding orbital BD*, the lone pairs LP and the anti-lone pairs LP*. The

two most prominent interactions in this molecule are LP-π^* and σ-σ^* interactions. This is in agreement with the studies of Unimuke et al., where he observed the major interaction in a pyrimidine ring to be the LP-π^* interaction. The comparison shows that, there is little or no effect on the interactions in different solvents. For instance, in acetone, the total stabilization energy DET of the interaction between the bonding donor orbital σ (C_{15}-H_{18}), σ (C_{15}-C_{18}) and σ (C_5-C_6) with the anti-bonding orbital σ^*(C_{16}-N_{22}), σ^*(C_{17}-C_{20}) and σ^* (C_1-C_6) equals 4.62 kcal/mol.

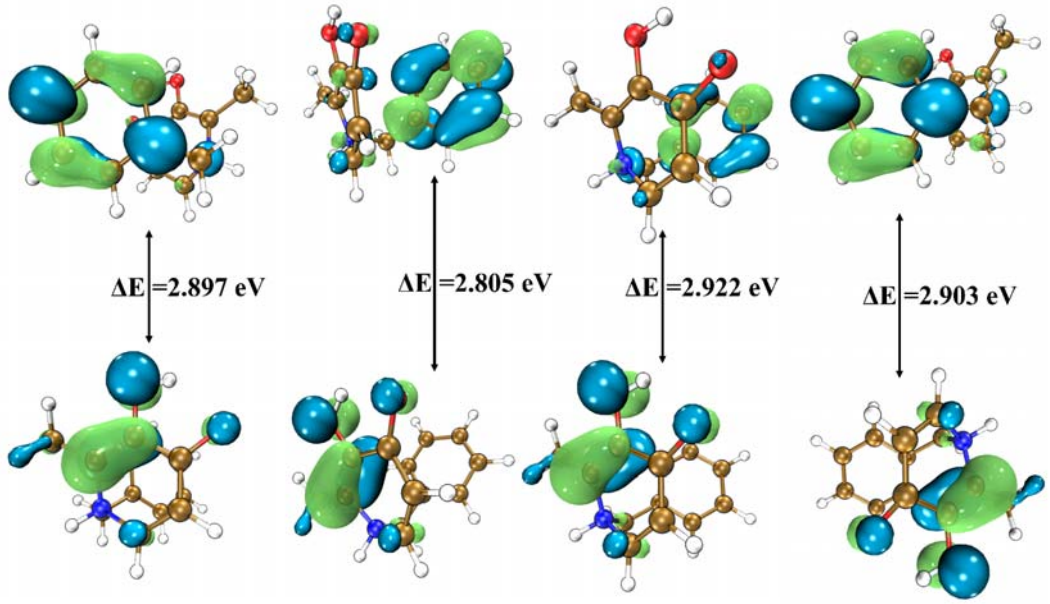

Figure 7: HOMO –LUMO plots for BHM in acetone, chloroform, ethanol and water.

In chloroform, the energy decreases a little towards 4.60 kcal/mol. Furthermore, in ethanol and water, Interactions between the bonding donor orbital with the antibonding orbital equals 4.63kcal/mol. Herein, the highest stabilization energy is observed between the LP π^* interactions with stabilization energies of 109.58, 106.62, 106.46 and 105.92kcal/mol for chloroform, acetone, ethanol, and water respectively. This obtained result is not in concord with the studies of Noureddine et al., where he observed the mean stabilization energy to be high between the BD to BD* than that of the LP (1) to BD*. The highest stabilization energy is found in chloroform while the least is found in water. Other possible interactions in this molecule include the π π^* (π C_5-C_6/ π^*C_1-C_2), π^* σ^*(π^*C_{16}-C_{19}/ σ^*C_{27}-H_{29}), LP (2) π^* (O24/ σ^*C_{19}-C_{20}) and LPσ^* ($LP_{(2)}O_2/\pi^*C_{16}$-C_{19}). Because of these interactions, there is significant intramolecular charge transfer, which stabilizes the molecule. Furthermore, high

stabilization energy resulting from non-bonding and bonding interactions between LP (2) O_{24}/ σ^*C_{19}-C_{20}, LP $_{(2)}$ O_2/π^*C_{16}-C_{19} and π C_5-C_6 / π^*C_1-C_2 were also observed.

3.2.2 Nonlinear optics (NLO) analysis

The non-linear optics describes the non-linearity of a material medium to the action of electromagnetic wave in an optic domain. Non-linear optics (NLO) has found use in telecommunications, optical data storage, and contemporary high-tech applications (41). Studies have shown that organic materials tend to have higher non-linear properties than inorganic molecules. The calculations of the polarizability of molecule can be carried out using the DFT theory. Herein, the NLO properties of BHM was carried out in four different solvents (ethanol, chloroform, acetone and water) employing DFT method at B3LYP/6-311++ G (d p) basis set in order to explain dipole moment, Static polarizability and static first hyperpolarizability of the studied compound. The first substance to have its NLO properties investigated was urea, which is frequently used as a benchmark for comparison. The total dipole is used to demonstrate the charge transfer within the molecule. The second microscopic source of the third order NLO response is thought to be the second hyperpolarizability. Through polarizability and first hyperpolarizability, a molecule's response to an electric field is demonstrated. The tensor component of polarizability can be used to determine this response and can be calculated using the following equations (6) – (7).

$$\alpha_{total} = 1/3(\alpha_{xx} +\alpha_{yy} +\alpha_{zz}) \quad (6)$$

$$\beta_{total} =(\beta_x +\beta_y + \beta_z)^{1/2} \quad (7)$$

Where,

$\beta_x= \beta_{xxx} + \beta_{xyy} +\beta_{xzz}$

$\beta_y= \beta_{yyy}+\beta_{yzz}+ \beta_{yxx}$

$\beta_z= \beta_{zzz}+\beta_{zxx}+ \beta_{zyy}$

Hence the equation is written as

$$\beta_{total} =[(\beta_{xxx} + \beta_{xyy} +\beta_{xzz})^2 +(\beta_{yyy}+\beta_{yzz}+ \beta_{yxx})^2 +(\beta_{zzz}+\beta_{zxx}+ \beta_{zyy})^2]^{1/2}. \quad (8)$$

Table 4: Second order perturbation energies of BHM in ethanol, water, acetone and chloroform calculated using B3LYP-GD3BJ/6-311++G (d. p) functional/basis set.

SOLVENT	TRANSITION	DONOR	ACCEPTOR	E^2 kcal/mol	F	E(j)-(i)
Ethanol	σ → σ*	σ C_{15}-H_{18}	σ* C_{16}-N_{22}	1.51	0.85	0.045
		σ C_{15}-H_{18}	σ* C_{17}-C_{20}	1.73	1.09	0.055
		σC_5-C_6	σ*C_1-C_6	1.39	1.28	0.053
				4.63		
	LP(1)→ π *	LP(1)C_{20}	π*C_{16}-C_{19}	37.09	0.15	0.106
		LP(1)C_{20}	π* C_{15}-C_{17}	69.37	0.13	0.125
				106.46		
Water	σ → σ*	σ C_{15}-H_{18}	σ* C_{16}-N_{22}	1.51	0.85	0.045
		σ C_{15}-H_{18}	σ* C_{17}-C_{20}	1.73	1.09	0.055
		σC_5-C_6	σ*C_1-C_6	1.39	1.28	0.053
				4.63		
	LP(1)→ π *	LP(1)C_{20}	π*C_{16}-C_{19}	36.98	0.15	0.106
		LP(1)C_{20}	π* C_{15}-C_{17}	68.94	0.13	0.125
				105.92		
Chloroform	σ → σ*	σ C_{15}-H_{18}	σ* C_{16}-N_{22}	1.50	0.85	0.045
		σ C_{15}-H_{18}	σ* C_{17}-C_{20}	1.70	1.09	0.055
		σC_5-C_6	σ*C_1-C_6	1.40	1.28	0.053
		E^2		**4.60**		
	LP(1)→ π *	LP(1)C_{20}	π*C_{16}-C_{19}	37.73	0.15	0.106
		LP(1)C_{20}	π* C_{15}-C_{17}	71.85	0.13	0.125
		E^2		**109.58**		
Acetone	σ → σ*	σ C_{15}-H_{18}	σ* C_{16}-N_{22}	1.50	0.85	0.045
		σ C_{15}-H_{18}	σ* C_{17}-C_{20}	1.73	1.09	0.055
		σC_5-C_6	σ*C_1-C_6	1.39	1.28	0.053
		E^2		**4.62**		
	LP(1)→ π *	LP(1)C_{20}	π*C_{16}-C_{19}	37.12	0.15	0.106
		LP(1)C_{20}	π* C_{15}-C_{17}	69.50	0.13	0.125
		E^2		**106.62**		

Table 5 shows the dipole moment, static polarizability, and hyperpolarizability of compound BHM in four distinct solvents. Based on these findings, water, had the greatest dipole moment values of 11.2720D, followed by ethanol with a value of 11.1028D, acetone (11.0511D) and chloroform (10.1454D). The dipole moment in decreasing order is expressed as water>ethanol>acetone>chloroform. The high dipole moment in water may be as a result of the polar nature of water. Higher hyperpolarizability values are found in molecules with narrow energy gaps and high static polarizability values. This assertion is found to be true in this study as water has a high static polarizability value of -93.9713 a.u and a corresponding higher

hyperpolarizability value of 90.7258 a.u. the lowest static polarizability value of -94.1394 a.u and corresponding low hyperpolarizability of 76.5779 a.u is observed in chloroform. The high hyperpolarizability observed in water may be due to charge transfer properties coming from the transition electron cloud from an electron donor region to an electron acceptor region (42, 43). The hyperpolarizability in decreasing order is water>ethanol>acetone>chloroform. Herein, it can be suggested that **BHM** has non-linear optics properties irrespective of the solvent and can be employed in various fields where its non-linear property may be required.

Table 5: Dipole moment, Static polarizability, Anisotropy and the Hyperpolarizability of BHM calculated at different solvents calculated at B3LYP-GD3BJ/ 6-311++ G (d p) level of theory.

Solvents	**Dipole moment**	**Static polarizability(a.u)**	**Anisotropy (a.u)**	**Hyperpolarizability (a.u)**
Acetone	11.051	-94.012	12.064	87.947
Chloroform	10.145	-94.139	11.451	76.577
Ethanol	11.102	-93.995	12.066	88.602
Water	11.272	-93.971	12.175	90.725

3.5 Molecular docking discussion

In addition to approaches undertaken to investigate the properties of BHM, its anticarcinogenic property was studied using in silico molecular docking, an approach which is applicable to a wide range of molecule groups such as protein-protein, protein-nucleic acid, protein-ligand etc. Essentially, molecular docking approach hinges on such intrinsic molecular properties such as biochemical affinity and specificity of a ligand to a receptor (44) to help elucidate and predict the nature of their biological interaction as may be required to further enhance an understanding of the pharmaceutical usefulness in terms of either comparative pharmacochemical advantage or parity of the ligand with reference to other medically recommended and pharmacologically established functionally similar drugs (45-48).

Notwithstanding the presence of other non-covalent intermolecular interactions including pi–pi stacking, pi-pi T shaped, pi-alkyl, carbon-hydrogen interactions and van der Waals interactions equally present in all the six protein-ligand interactions, the most important premise on which the discussion is based is the conventional hydrogen bond interactions present in the receptor-ligand complex as this has been repeatedly shown to have the greatest impact to receptor-ligand interactions (34-36, 41, 49). It is evident the difference between the average ligand pair (i.e. BHM and complementary standard drug) binding affinities for each protein considered is within close range. This is in no way surprising as BHM is not structurally

analogous to TRA, CLO or DOC hence their reactivity cannot be the perfectly the same. Synchronously, a close investigation of the comparative best pose binding affinity (Kcal/mol) and bond length of analogous conventional hydrogen bonds exactly the same in both BHM and any juxtaposed standard drug leads to the sound deduction that BHM has anticarcinogenic potency. This is especially true for leukemia. Furthermore, as clearly shown in the 2D diagrams, the bond distance for donor-acceptor species in analogous conventional hydrogen bonds such SER:A:583 in BHM and TRA is lesser in BHM compared to TRA thereby indicating greater reactivity potential as basically the fundamental premise that the shorter the bond length the greater the reactivity (50, 51) holds true in this case.

With 6qpn, the affinity of -4.2kcal/mol of BHM was mainly due to favorable hydrogen bond at SER:A:583 with a bond length of 3.40 while TRA had a higher affinity of -4.9kcal/mol with two hydrogen bonds established at the binding site namely: SER:A:583 and GLY:A:540 with bond lengths of 3.67 and 2.78 respectively. Two basic observations can be made namely: the difference in affinity is small (-0.7kcal/mol) and BNM has a shorter bond length for SER:A:583 with a difference of 0.27 which gives it a comparative biochemical reactivity at this particular site (52-55).

Table 6: Binding energies and average binding affinities (BA) (kcal/mol) of the interactions between the cancer proteins with BHM and with their corresponding medically recommended drugs: trastuzumab (TRA), clolar (CLO) for leukemia and docetaxel (DOC) for lung cancer as obtained from Autodock Vina**.**

MODE	ESOPAHGEAL CANCER		LEUKEMIA		LUNG CANCER	
	Binding affinity (Kcal/mol)	Binding affinity (Kcal/mol)	Binding affinity (Kcal/mol)	Binding affinity (Kcal/mol)	Binding affinity (Kcal/mol)	Binding affinity (Kcal/mol)
	BNM-6qpn	TRA-6qpn	BNM-4p5e	CLO-4p5e	BNM-7vov	DOC-7vov
1	-4.2	-4.9	-5.8	-5.8	-5.3	-5.6
2	-4.2	-4.8	-5.5	-5.6	-5.0	-5.5
3	-4.1	-4.7	-5.3	-5.6	-4.7	-5.5
4	-4.1	-4.6	-5.3	-5.5	-4.7	-5.4
5	-3.7	-4.4	-5.3	-5.3	-4.6	-5.4
6	-3.6	-4.4	-5.2	-5.3	-4.6	-5.3
7	-3.4	-4.4	-5.2	-5.3	-4.5	-5.2
8	-3.4	-4.3	-5.0	-5.2	-4.4	-5.2
9	-3.3	-4.1	-5.0	-5.2	-4.3	-5.2
			Mean binding affinity			
	-3.8	-4.5	-5.3	-5.4	-4.7	-5.4

A similar trend of BHM having a shorter bond length at analogous hydrogen bond sites is equally obvious in 4p5e and 7vov as presented in **Table 6**. In the interaction with 4p5e, the binding affinities are the same for both BHM and CLO this can be accounted for by the presence of five van der Waals interaction in CLO [ALA:B:60, ALA:B:59, ARG:B:36, SER:B:44 and GLU:B:55] and none in BHM which evidently lowered its affinity thereby reducing the impact of the other three conventional hydrogen bonds in CLO: ARG:B:47 (4.93, 6.11, 6.65). In the interaction with 7vov, DOC had a slightly higher binding affinity at the best pose with a difference of -0.3kcal/mol. The presence of the van der Waals forces in both 7vov-BNM and 7vov-DOC interactions lowered the net binding affinity. Furthermore, the amino acid residue for BHM had only one hydrogen bond interaction at the active site whereas DOC had five. Additionally, as earlier hinted, BHM had a shorter bond distance at the ASN:A:58 interaction with a difference of 0.1 which also adds in no little way to its anticarcinogenic potency.

Table 7: The binding affinities and amino acid residues of the best pose of BHM and the standard drugs (1=TRA, 2=CLO and 3=DOC) with the proteins as utilized.

RECEPTOR DETAILS		**LIGAND (BHM) DEETAILS**		**STANDARD DRUGS[1,2,3]**	
Cancer type	**PDB code**	**Binding affinity of best pose (Kcal/mol)**	**Amino acid residue**	**Binding affinity of best pose (Kcal/mol)**	**Amino acid residue**
Esophageal cancer	6qpn	-4.2	A:SER:583 (3.40)	-4.9	A:SER:583 (3.67); A:GLY:540 (2.78)
Leukemia	4p5e	-5.8	B:ARG:47 (4.88)	-5.8	B:GLY:40 (3.89); B:ARG:47 (4.93, 6.11, 6.65)
Lung cancer	7vov	-5.3	A:ASN:58 (5.03)	-5.6	A:ASN:58 (5.04); A:LYS:62 (4.08, 4.92); A:PHE:61 (4.79, 5.88)

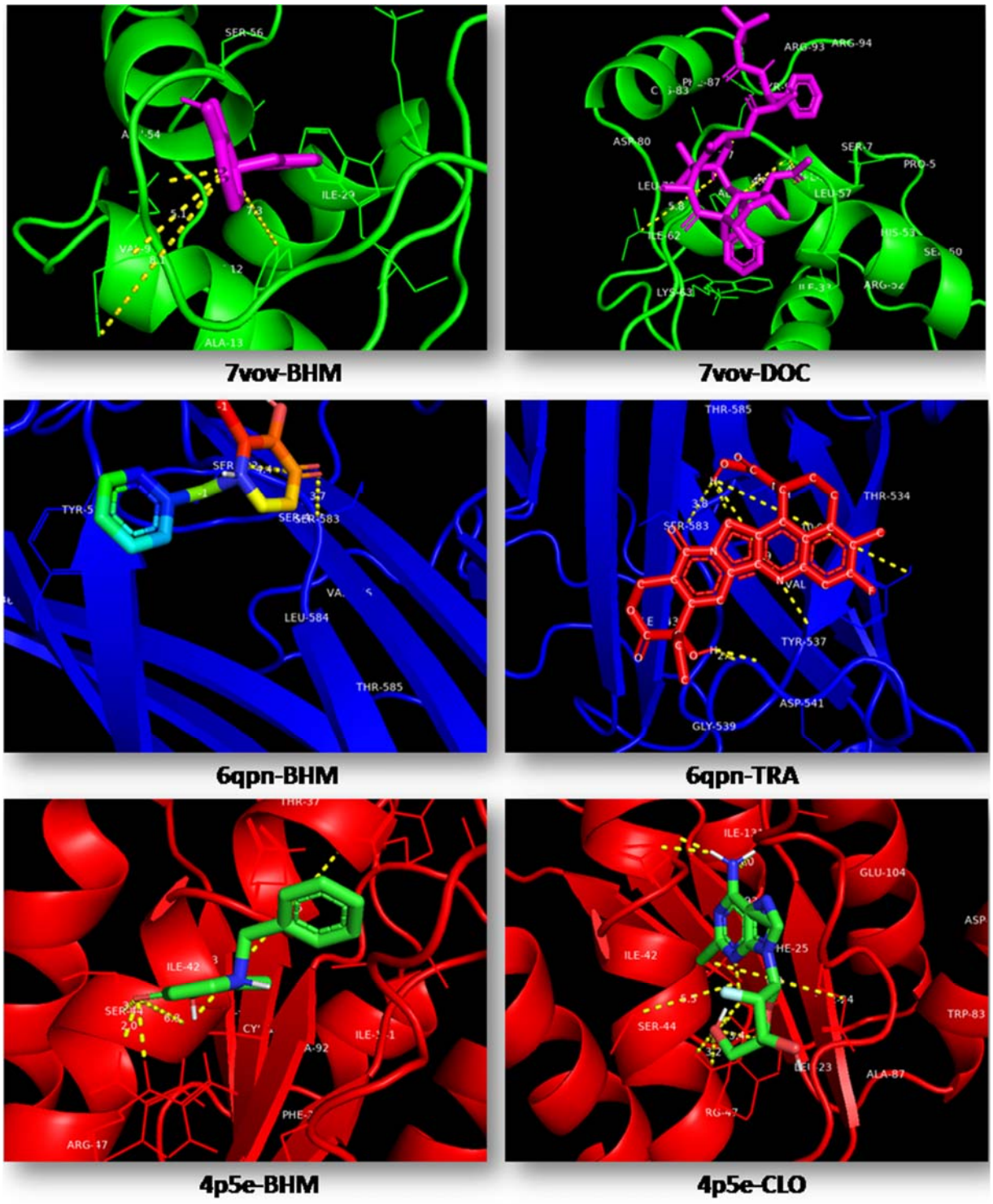

Figure 8: The 3D diagrams of the molecular docking interactions of the three proteins with BHM and the complementary standard drugs.

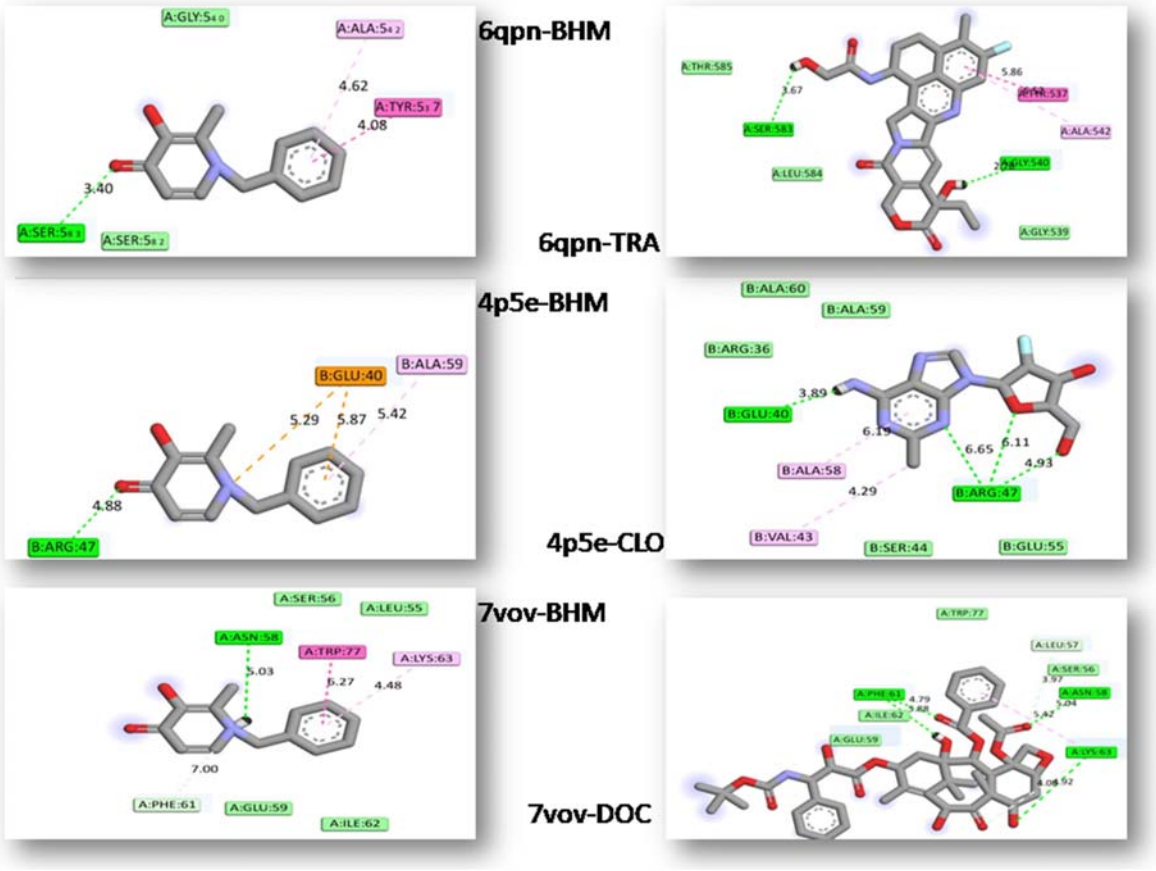

Figure 9: The 2D diagrams of the molecular docking interactions of the three proteins with BHM and the complementary standard drugs.

4.0 Conclusions

This research work incorporated both experimental and theoretical approaches to ensure a detailed investigation of the structure and nature of BHM. The experimental synthesis and isolation of the compound was reported in addition to a detailed investigation of the structural properties, electronic properties (FMO, NLO and NBO) and spectroscopic property (FT-IR) all calculated using the density functional theory method with the B3LYP functional and 6-3++G(d,p) basis set in addition to in-silico molecular docking studies to determine the anticarcinogenic activity of BHM. The structural properties showed the lattice constant to range from 1.391Å – 1.477Å and 119.934^0 – 120.451^0 for theoretical and 1.359Å – 1.440 Å; and 115.211^0 to 122.431^0 for the experimental. Furthermore, the FMO analysis showed that BHM had HOMO and LUMO values ranging from – (3.869 to 3.956) eV and – (1.034 to 1.063) eV respectively with BHM having the highest HOMO energy in water and the lowest LUMO in the same solvent. The NLO result showed that the highest and lowest values of dipole moment,

static polarizability, anisotropy and hyperpolarizability were observed in water and chloroform respectively. The result of the NBO analysis shows that the highest stabilization energies across the four solvents: ethanol, water, chloroform and acetone were 106.46 kcal/mol, 105.92 kcal/mol, 109.58 kcal/mol and 106.62 kcal/mol respectively and all due to the $LP_{(1)} \rightarrow \pi^*$ transition across all four solvents with the donor and acceptor species in the solvent order previously established being $LP_{(1)}C_{20} \rightarrow \pi^*C_{16}\text{-}C_{19}$ and $LP_{(1)}C_{20} \rightarrow \pi^*C_{15}\text{-}C_{17}$ in each case thereby showing that the highest stabilization energy of BHM was in chloroform. The Hirschfield Surface analysis showed the major intermolecular interactions to stem from H---H (54%), C---H (11.5%) and O---H (10.5%) while the strong intramolecular interaction was due to the H---O bond.The spectroscopic analysis showed the major functional groups which peaked at the functional group region were as follows: ν_sOH at 3178.40 in the experimental and 3348.90 in chloroform; ν_sNH at 3054.50 in the experimental and 3306.45 in chloroform; ν_sCH at 2940 in the experimental and 2893.55 in chloroform as well thereby confirming that the scaled theoretical wavenumbers in chloroform were closest to the experimental. Other major groups include β_{asym}CH, ν_sCC and γ CH. Finally, the molecular docking results showed that BHM had mean binding affinities of -3.8, -5.3 and -4.7 thereby establishing that its anticarcinogenic potential was greatest against the leukemia protein 4p5e.

Acknowledgment: We would like to thank the National Research Foundation South Africa (Grant No. 129468), Tshwane University of Technology and the University of Pretoria for institutional and financial support. We appreciate the Centre for high-performance computing for the computational resources.

Conflict of interest: All authors unanimously declare zero conflict of interest

References

1. Tariq A, Nazir S, Arshad AW, Nawaz F, Ayub K, Iqbal J. DFT study of the therapeutic potential of phosphorene as a new drug-delivery system to treat cancer. RSC Advances. 2019;9(42):24325-32.
2. Oyewole RO, Oyebamiji AK, Semire B. Theoretical calculations of molecular descriptors for anticancer activities of 1, 2, 3-triazole-pyrimidine derivatives against gastric cancer cell line (MGC-803): DFT, QSAR and docking approaches. Heliyon. 2020;6(5):e03926.
3. Munir I, Perveen M, Nazir S, Khera RA, Ayub AR, Ayub K, et al. Therapeutic potential of graphyne as a new drug-delivery system for daunorubicin to treat cancer: A DFT study. Journal of Molecular Liquids. 2021;336:116327.
4. Rigaku O. CrysAlis PRO Software system. Oxford, UK: Rigaku Corporation; 2018.
5. Sheldrick G. SHELXT - Integrated space-group and crystal-structure determination. Acta Crystallographica Section A. 2015;71(1):3-8.
6. Becke AD. Density-functional exchange-energy approximation with correct asymptotic behavior. Phys Rev A Gen Phys. 1988;38(6):3098-100.

7. Frisch MJ, Trucks GW, Schlegel HB, Scuseria GE, Robb MA, Cheeseman JR, et al. Gaussian 16 Rev. C.01. Wallingford, CT2016.
8. Spackman PR, Turner MJ, McKinnon JJ, Wolff SK, Grimwood DJ, Jayatilaka D, et al. CrystalExplorer: a program for Hirshfeld surface analysis, visualization and quantitative analysis of molecular crystals. Journal of applied crystallography. 2021;54(Pt 3):1006-11.
9. Lu T, Chen F. Multiwfn: A multifunctional wavefunction analyzer. Journal of Computational Chemistry. 2012;33(5):580-92.
10. Choi Y, Luo Y, Lee S, Jin H, Yoon HJ, Hahn Y, et al. FOXL2 and FOXA1 cooperatively assemble on the TP53 promoter in alternative dimer configurations. Nucleic Acids Res. 2022;50(15):8929-46.
11. Amiable C, Paoletti J, Haouz A, Padilla A, Labesse G, Kaminski PA, et al. 6-(Hetero)Arylpurine nucleotides as inhibitors of the oncogenic target DNPH1: synthesis, structural studies and cytotoxic activities. European journal of medicinal chemistry. 2014;85:418-37.
12. Baker AT, Davies JA, Bates EA, Moses E, Mundy RM, Marlow G, et al. The Fiber Knob Protein of Human Adenovirus Type 49 Mediates Highly Efficient and Promiscuous Infection of Cancer Cell Lines Using a Novel Cell Entry Mechanism. J Virol. 2021;95(4).
13. Valdés-Tresanco MS, Valdés-Tresanco ME, Valiente PA, Moreno E. AMDock: a versatile graphical tool for assisting molecular docking with Autodock Vina and Autodock4. Biol Direct. 2020;15(1):12.
14. Kiran K, editor Synthesis, Characterization and Antibacterial Activity of Cu(II), Zn(II) Ternary Complexes with Maltol and Glycylglycine2014.
15. Naqvi SS, Anwer H, Siddiqui A, Zohra RR, Ali SA, Shah MR, et al. Novel Synthesis of Maltol Capped Copper Nanoparticles and Their Synergistic Antibacterial Activity with Antibiotics. Plasmonics. 2021;16(6):1915-28.
16. Waser J, Pauling L. Compressibilities, Force Constants, and Interatomic Distances of the Elements in the Solid State. The Journal of Chemical Physics. 1950;18(5):747-53.
17. Dege N, Gökce H, Doğan OE, Alpaslan G, Ağar T, Muthu S, et al. Quantum computational, spectroscopic investigations on N-(2-((2-chloro-4,5-dicyanophenyl)amino)ethyl)-4-methylbenzenesulfonamide by DFT/TD-DFT with different solvents, molecular docking and drug-likeness researches. Colloids and Surfaces A: Physicochemical and Engineering Aspects. 2022;638:128311.
18. Stephenson JC, Wood RE, Moore CB. Near-Resonant Energy Transfer between Infrared-Active Vibrations. The Journal of Chemical Physics. 1968;48(10):4790-1.
19. Fabian J, Herzog K. Post–Hartree–Fock MP2 and density functional theory derived structure and vibrations of 1,2-dithiole-2-thione and 1,2-dithiole-3-one. Vibrational Spectroscopy. 1998;16(1):77-83.
20. Krishnakumar V, Prabavathi N. Simulation of IR and Raman spectral based on scaled DFT force fields: A case study of 2-amino 4-hydroxy 6-trifluoromethylpyrimidine, with emphasis on band assignment. Spectrochimica Acta Part A: Molecular and Biomolecular Spectroscopy. 2008;71(2):449-57.
21. Bouteiller Y, Gillet JC, Grégoire G, Schermann JP. Transferable specific scaling factors for interpretation of infrared spectra of biomolecules from density functional theory. J Phys Chem A. 2008;112(46):11656-60.
22. Sundaraganesan N, Joshua BD. Vibrational spectra and fundamental structural assignments from HF and DFT calculations of methyl benzoate. Spectrochim Acta A Mol Biomol Spectrosc. 2007;68(3):771-7.
23. Tekin N, Namli H, Turhan O. Solvents effect on infrared spectra of 1,3-indanedione in organic solvents. Vibrational Spectroscopy. 2005;39:214-9.
24. Kosower EM. The Effect of Solvent on Spectra. I. A New Empirical Measure of Solvent Polarity: Z-Values. Journal of the American Chemical Society. 1958;80:3253-60.
25. Schuler MJ, Hofer TS, Morisawa Y, Futami Y, Huck CW, Ozaki Y. Solvation effects on wavenumbers and absorption intensities of the OH-stretch vibration in phenolic compounds –

electrical- and mechanical anharmonicity via a combined DFT/Numerov approach. Physical Chemistry Chemical Physics. 2020;22(23):13017-29.
26. Tommasini M, Lucotti A, Alfè M, Ciajolo A, Zerbi G. Fingerprints of polycyclic aromatic hydrocarbons (PAHs) in infrared absorption spectroscopy. Spectrochim Acta A Mol Biomol Spectrosc. 2016;152:134-48.
27. Hopewell JL, George GA, Hill DJT. Quantitative analysis of bismaleimide-diamine thermosets using near infrared spectroscopy. Polymer. 2000;41(23):8221-9.
28. Bauschlicher CW, Langhoff SR. The Calculation of Accurate Harmonic Frequencies of Large Molecules: The Polycyclic Aromatic Hydrocarbons, a Case Study. Spectrochimica Acta Part A: Molecular and Biomolecular Spectroscopy. 1997;53:1225-40.
29. Makhlouf J, Louis H, Benjamin I, Ukwenya E, Valkonen A, Smirani W. Single crystal investigations, spectral analysis, DFT studies, antioxidants, and molecular docking investigations of novel hexaisothiocyanato chromate complex. Journal of Molecular Structure. 2023;1272:134223.
30. Kansız S, Tolan A, Azam M, Dege N, Alam M, Sert Y, et al. Acesulfame based Co(II) complex: Synthesis, structural investigations, solvatochromism, Hirshfeld surface analysis and molecular docking studies. Polyhedron. 2022;218:115762.
31. Oueslati Y, Kansız S, Dege N, de la Torre Paredes C, Llopis-Lorente A, Martínez-Máñez R, et al. Growth, crystal structure, Hirshfeld surface analysis, DFT studies, physicochemical characterization, and cytotoxicity assays of novel organic triphosphate. J Mol Model. 2022;28(3):65.
32. Obu QS, Louis H, Odey JO, Eko IJ, Abdullahi S, Ntui TN, et al. Synthesis, spectra (FT-IR, NMR) investigations, DFT study, in silico ADMET and Molecular docking analysis of 2-amino-4-(4-aminophenyl)thiophene-3-carbonitrile as a potential anti-tubercular agent. Journal of Molecular Structure. 2021;1244:130880.
33. Asogwa FC, Agwamba EC, Louis H, Muozie MC, Benjamin I, Gber TE, et al. Structural benchmarking, density functional theory simulation, spectroscopic investigation and molecular docking of N-(1H-pyrrol-2-yl) methylene)-4-methylaniline as castration-resistant prostate cancer chemotherapeutic agent. Chemical Physics Impact. 2022;5:100091.
34. Reed AE, Curtiss LA, Weinhold F. Intermolecular interactions from a natural bond orbital, donor-acceptor viewpoint. Chemical Reviews. 1988;88(6):899-926.
35. Wei K, Louis H, Emori W, Idante PS, Agwamba EC, Cheng C-R, et al. Antispasmodic activity of carnosic acid extracted from rosmarinus officinalis: Isolation, spectroscopic characterization, DFT studies, and in silico molecular docking investigations. Journal of Molecular Structure. 2022;1260:132795.
36. Agwamba EC, Benjamin I, Louis H, Udoikono AD, Igbalagh AT, Egemonye TC, et al. Antitubercolusic Potential of Amino-(formylphenyl) Diazenyl-Hydroxyl and Nitro-Substituted Naphthalene-Sulfonic Acid Derivatives: Experimental and Theoretical Investigations. Chemistry Africa. 2022;5(5):1451-67.
37. Eno EA, Louis H, Unimuke TO, Gber TE, Akpanke JA, Amodu IO, et al. Modeling of Re(I) tricarbonyl complexes against SARS-CoV-2 receptor via DFT, in-silico molecular docking, and QSAR. Chemical Physics Impact. 2022;5:100105.
38. Unimuke TO, Louis H, Eno EA, Agwamba EC, Adeyinka AS. Meta-Hybrid Density Functional Theory Prediction of the Reactivity, Stability, and IGM of Azepane, Oxepane, Thiepane, and Halogenated Cycloheptane. ACS Omega. 2022;7(16):13704-20.
39. Louis H, Charlie DE, Amodu IO, Benjamin I, Gber TE, Agwamba EC, et al. Probing the Reactions of Thiourea (CH4N2S) with Metals (X = Au, Hf, Hg, Ir, Os, W, Pt, and Re) Anchored on Fullerene Surfaces (C59X). ACS Omega. 2022;7(39):35118-35.
40. Glendening ED, Landis CR, Weinhold F. Natural bond orbital methods. WIREs Computational Molecular Science. 2012;2(1):1-42.
41. Udoikono AD, Louis H, Eno EA, Agwamba EC, Unimuke TO, Igbalagh AT, et al. Reactive azo compounds as a potential chemotherapy drugs in the treatment of malignant glioblastoma (GBM): Experimental and theoretical studies. Journal of Photochemistry and Photobiology. 2022;10:100116.

42. Prathiksha G, Thangaiyan P, Bakht M, Thomas R. Understanding the solvation dynamics of metformin in water using theoretical tools. Journal of Molecular Liquids. 2022;362:119678.
43. Pooventhiran T, Gangadharappa BS, Abu Ali OA, Thomas R, Saleh DI. Study of the structural features and solvent effects using ab initio molecular dynamics and energy decomposition analysis of atogepant in water and ammonia. Journal of Molecular Liquids. 2022;352:118672.
44. Geethapriya J, Shanthidevi A, Arivazhagan M, Elangovan N, Thomas R. Synthesis, structural, DFT, quantum chemical modeling and molecular docking studies of (E)-4-(((5-methylfuran-2-yl)methylene)amino) benzenesulfonamide from 5-methyl-2-furaldehyde and sulfanilamide. Journal of the Indian Chemical Society. 2022;99:100418.
45. Thomas R, Hossain M, Mary YS, Resmi KS, Armaković S, Armaković SJ, et al. Spectroscopic analysis and molecular docking of imidazole derivatives and investigation of its reactive properties by DFT and molecular dynamics simulations. Journal of Molecular Structure. 2018;1158:156-75.
46. Muthukumar R, Karnan M, Elangovan N, Karunanidhi M, Thomas R. Synthesis, spectral analysis, antibacterial activity, quantum chemical studies and supporting molecular docking of Schiff base (E)-4-((4-bromobenzylidene) amino)benzenesulfonamide. Journal of the Indian Chemical Society. 2022;99(5):100405.
47. Benjamin I, Udoikono AD, Louis H, Agwamba EC, Unimuke TO, Owen AE, et al. Antimalarial potential of naphthalene-sulfonic acid derivatives: Molecular electronic properties, vibrational assignments, and in-silico molecular docking studies. Journal of Molecular Structure. 2022;1264:133298.
48. Eno EA, Mbonu JI, Louis H, Patrick-Inezi FS, Gber TE, Unimuke TO, et al. Antimicrobial activities of 1-phenyl-3-methyl-4-trichloroacetyl-pyrazolone: Experimental, DFT studies, and molecular docking investigation. Journal of the Indian Chemical Society. 2022;99(7):100524.
49. Ugwu D, Asogwa F, Louis H, Uchenna E, Gber T, Chinasa U, et al. Synthesis, vibrational analysis, molecular property investigation, and molecular docking of new benzenesulphonamide-based carboxamide derivatives against Plasmodium falciparum. Journal of Molecular Structure. 2022;1269:133796.
50. Jiang W, Zhang L, Zhang L. Reactivity of a mixed methyl–aminobenzyl guanidinate lutetium complex towards iPrN ✓ C ✓ NiPr, CS2 and Ph2PH. Dalton Transactions. 2022;51(33):12650-60.
51. Allen FH, Kirby AJ. Bond length and reactivity. Variable length of the carbon-oxygen single bond. Journal of the American Chemical Society. 1984;106(21):6197-200.
52. Mohammed HA, Sert Y, Albayati MR, Dege N, Şen F. Structure Elucidation, Hirshfeld Surface Analysis, Molecular Docking and Computational Studies of a Jahn-Teller Distorted Octahedral Cobalt (II) Complex with Saccharin Ligand. Polycyclic Aromatic Compounds. 2022:1-11.
53. Mahmoudi G, Sahli S, Tamer Ö, Berrin Çınar E, Böhme U, Dege N, et al. Investigation on crystal structure, spectral FT-IR analysis, DFT and molecular docking studies of a novel complex with the N'-(pyridin-2-ylmethylene)nicotinohydrazide. Journal of Molecular Structure. 2022;1269:133741.
54. Benjamin I, Gber TE, Louis H, Ntui TN, Oyo-Ita EI, Unimuke TO, et al. Modelling of Aminothiophene-Carbonitrile Derivatives as Potential Drug Candidates for Hepatitis B and C. Iranian Journal of Science and Technology, Transactions A: Science. 2022;46(5):1399-412.
55. Eno EA, Louis H, Ekoja P, Benjamin I, Adalikwu SA, Orosun MM, et al. Experimental and computational modeling of the biological activity of benzaldehyde sulphur trioxide as a potential drug for the treatment of Alzheimer disease. Journal of the Indian Chemical Society. 2022;99(7):100532.
56. Roy, D.; Keith, T. A.; Millam, J. M. GaussView, version 6; Semichem Inc.: Shawnee Mission, KS, 2016.
57. M.J. Frisch , G.W. Trucks , H.B. Schlegel , G.E. Scuseria , M.A. Robb , J.R. Cheese- man , G. Scalmani , V. Barone , B. Mennucci , G.A. Petersson , H. Nakatsuji , M. Caricato , X. Li , H.P. Hratchian , A.F. Izmaylov , J. Bloino , G. Zheng , J.L. Son- nenberg , M. Hada , M. Ehara , K. Toyota , R. Fukuda , J. Hasegawa , M. Ishida , T. Nakajima , Y. Honda , O. Kitao , H. Nakai , T. Vreven , J.A. Montgomery Jr , J.E. Peralta , F. Ogliaro , M. Bearpark , J.J. Heyd , E. Brothers , K.N. Kudin , V.N. Staroverov , R. Kobayashi , J. Normand , K. Raghavachari , A. Rendell , J.C. Bu- rant , S.S. Iyengar , J. Tomasi , M. Cossi , N. Rega ,

J.M. Millam , M. Klene , J.E. Knox , J.B. Cross , V. Bakken , C. Adamo , J. Jaramillo , R. Gomperts , R.E. Stratmann , O. Yazyev , A.J. Austin , R. Cammi , C. Pomelli , J.W. Ochterski , R.L. Martin , K. Mo- rokuma , V.G. Zakrzewski , G.A. Voth , P. Salvador , J.J. Dannenberg , S. Dapprich , A.D. Daniels , Ö. Farkas , J.B. Foresman , J.V. Ortiz , J. Cioslowski , D.J. Fox , Gaussian 09, Gaussian, Inc., Wallingford CT, 2009.

58. Chemcraft, V. 1.8; Graphical Software for Visualization of Quantum Chemistry Computations.

59. OriginPro 2018 (64-bit) SR1 b9.5.1.195 (Academic) (OriginLab Corporation, Northampton, MA).

40. Schrodinger, L. L. C. (2008). The PyMOL Molecular Graphics System, Version 1.2 r3pre. Schrodinger LLC, New York, NY.

61. Visualizer, D. S. (2020). v21. 1.0. 20298. BIOVIA: San Diego, CA, USA.